

# CONCEPTUAL DESIGN OF HYDROGEN-POWERED AIRCRAFT: HIGH ASPECT RATIO WINGS AND FLOATING WINGTIPS

Fintan Healy<sup>1</sup>, Huaiyuan Gu<sup>1</sup>, Djamel Rezgui<sup>1</sup> & Jonathan Cooper<sup>1</sup>

<sup>1</sup>University of Bristol, Bristol, United Kingdom, BS8 1TR

#### **Abstract**

Hydrogen-powered aircraft present a promising solution to mitigate the aviation industry's environmental impact by eliminating in-flight carbon emissions and significantly reducing the production of nitrogen oxides (NOx). This study focuses on the conceptual design of hydrogen-powered aircraft featuring high aspect ratio wings (HARW) and floating wingtips. Using liquid hydrogen (LH<sub>2</sub>) as a fuel source introduces unique storage and structural design challenges, as the reduced energy density necessitates larger fuel tanks and results in fuel-free or 'dry' wings. These factors influence the optimal aspect ratio and fuel economy of an aircraft. This paper uses a conceptual sizing algorithm tailored for hydrogen-powered aircraft to examine the potential benefits of incorporating a semi-aeroelastic hinge (SAH) to mitigate loads during gust encounters and manoeuvres. The sizing algorithm uses aeroelastic simulations to estimate the loads during manoeuvres, gust and turbulence encounters. It shows that a SAH can lead to a 20% reduction in wing mass and a 5% improvement in the fuel economy of an aircraft.

Keywords: Floating Wingtips, Hydrogen-Powered Aircraft, Conceptual Design, Aeroelasticity

### 1. Introduction

Hydrogen-powered aircraft offer a promising avenue to reduce the aviation industry's climate impact, with the use of hydrogen eliminating in-flight carbon emissions and reducing the production of nitrogen oxides  $(NO_x)$  [2]. In particular, the cryogenic storage of liquid hydrogen and its combustion in turbofan engines holds significant potential for medium to long-range commercial flights. However, the cost per unit energy of  $LH_2$  will likely remain higher than that of existing kerosene fuels for the foreseeable future [2]. Therefore, the fuel efficiency of future aircraft must be increased to maintain similar operating costs to those of existing designs. To this end, future aircraft designs will likely include much higher aspect ratio wings (HARW) to reduce lift-induced drag and the amount of fuel required on a typical mission.

However, increasing an aircraft's wingspan is a challenge from a structural perspective, as it requires more material to support the increased loads. Additionally, increasing the aspect ratio can affect ground operations, with existing infrastructure at many airports - such as gate, runway and taxiway separation - only capable of servicing aircraft up to a specific wingspan. For this reason, aircraft with HARWs will likely incorporate folding wingtips (such as seen on the Boeing B777-X) to reduce their span whilst on the ground, further increasing the weight penalty of HARWs.

These increases in the wing mass require more lift (and, therefore, drag) to support in flight. This trade-off typically leads to an optimal aspect ratio at which the increased mass of further expanding the wingspan outweighs the reduction in induced drag [14, 25].

In kerosene-powered aircraft, fuel is typically stored within the wing. The mass of this fuel provides inertial relief, reducing the maximum loads seen during manoeuvres and gust encounters, which mitigates the required increase in wing mass with aspect ratio. For hydrogen-powered aircraft, the lower energy density of liquid hydrogen necessitates larger fuel stores within the aircraft structure. Furthermore, minimising the surface-to-volume ratio of these fuel tanks is crucial as this reduces the

tank's weight and the heat flux between the cryogenic liquid and the outside environment. For these reasons, most studies aim to place cylindrical tanks at the front, rear or above the passenger cabin [2] - resulting in fuel-free (or 'dry') wings. This loss of inertial relief increases the required mass of the wing structure, meaning hydrogen-powered aircraft will likely have a lower optimal aspect ratio and, therefore, a worse overall fuel economy when compared to kerosene-powered configurations.

As previously mentioned, sizing of the wing structure is generally determined by the worst-case loads (such as during manoeuvres, gusts, or turbulence encounters), which may only occur once during the lifetime of the airframe. To help mitigate these loads, devices that alter the lift distribution of the aircraft during these worst-case scenarios are of interest to aircraft designers. The basic premise of manoeuvre load alleviation (MLA) or gust load alleviation (GLA) devices is to alter the lift distribution of the wing to move loads inboard. Current implementations can be split into two broad categories: active and passive systems. Active systems (of which Regan and Jutte [36] provide a thorough review) typically create a control loop between sensor data and control surfaces already present on aircraft (such as spoilers and ailerons) [18, 23, 39]. Passive load alleviation systems remove the need for active control but generally rely on fluid-structure interactions and hence can only be optimised for small regions of a flight envelope, with the classic example of this being aeroelastic tailoring [37, 44]. Many other novel load alleviation systems have been proposed. However, there is typically a trade-off between the cost, complexity and, most importantly, the weight of including such a mechanism and its associated benefits. However, in the case of ground folding wingtips (GFWTs) (such as those used by the Boeing 777X), whilst these mechanisms are currently only operated on the ground, their mass has already been justified, raising the question of whether such a device could also be utilised in flight for load alleviation.

One such device is the flared floating wingtip (FFWT) [18, 21, 25, 27]. As shown in Fig. 1, this device consists of a GFWT in which the hinge line is rotated so that it is no longer parallel with the oncoming flow, with the magnitude of this rotation being defined as the flare angle,  $\Lambda$ . In this configuration, an increase in the fold angle,  $\theta$ , decreases the local angle of attack (AoA), and vice versa in the other direction. Therefore, when an FFWT is free to rotate, the fold angle tends to an equilibrium position, about which the aerodynamic and gravitational moments balance and the system is statically stable. During cruise, an FFWT 'locked' at a zero-degree fold angle would typically produce more lift than its weight. However, if the wingtip were 'released' and allowed to rotate freely, it would fold upwards, reducing the local AoA and, therefore, lift generated by the wingtip. This reduction in lift moves the centre of pressure of the entire wing inboard, leading to a reduction in loads. However, this alteration of the lift distribution also decreases an aircraft's overall aerodynamic efficiency. Therefore, concepts looking to utilize this technology, such as Airbus's upcoming extra high-performance wing demonstrator<sup>1</sup>, aim to use a so-called semi-aeroelastic hinge (SAH) [15, 25, 28]. This device allows the FFWT to be in either a 'fixed' state where the wingtip is rigidly connected to the inner wing or a 'free' state where the wingtips are free to rotate about the hinges. Therefore, the wingtip could be locked during cruise for optimal fuel economy, whilst unlocked during manoeuvres and gust encounters to reduce the peak wing loading. Multiple researchers have verified the possible load alleviation capabilities of the SAH either numerically or experimentally [12, 17, 21, 22], and a previous conceptual sizing study by the authors indicated that FFWTs could reduce the wing box mass of a kerosene-powered, A320-like, aircraft by up to 30% [25]. However, this study only altered the mass of the wing structure and did not consider the aircraft-level changes required to support this additional mass.

This paper considers the sizing of a medium-sized regional aircraft using a tool tailored for hydrogen-powered aircraft with high aspect-ratio wings. The sizing algorithm uses a combination of class-I and class-II sizing methodologies [41] to estimate the geometry and mass of a tube and wing configuration. The mass of most of the aircraft components is estimated using empirical relations; however, the mass of the wing structure is estimated using numerical simulations of manoeuvres and gust encounters (with the latter typically omitted in conceptual sizing studies). This methodology allows the benefits of a SAH to be considered at an aircraft level and highlights the impact of hydrogen-powered aircraft on the sizing of HARWs.

<sup>&</sup>lt;sup>1</sup>https://www.airbus.com/en/newsroom/press-releases/2021-09-airbus-launches-extra-high-performance [retrieved 06/06/2024]

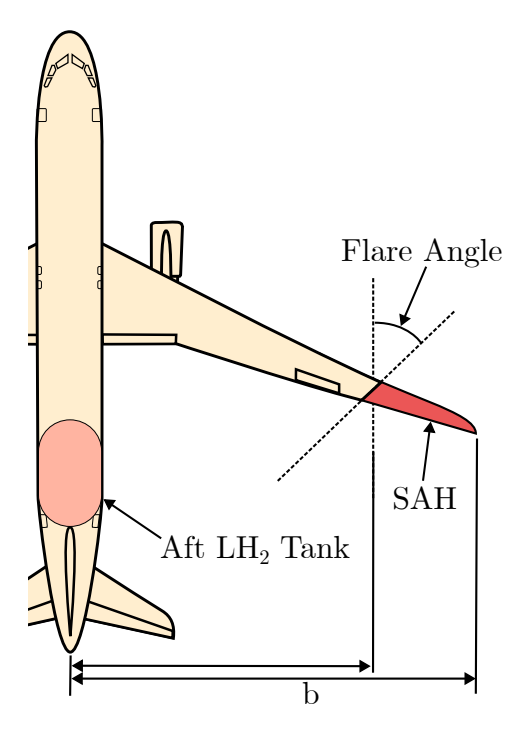


Figure 1 – Representation of the key configuration variables explored during this paper.

Table 1 – Top Level Aircraft Requirements For an A320-like Aircraft

Parameter	Value	Unit
PAX (single class)	180	-
Maximum Payload	19.3	t
Harmonic Range	2450	nm
Cruise Altitude	34000	ft
Cruise Mach	0.78	-
Maximum Wingspan	36	m
$V_{climb}$ [CAS]	150	m/s
$V_{app}$ [CAS]	129	m/s
$(T/W)_{TO}$	0.31	-
$M_{Lnd}/S$	550.7	$kg/m^2$

Table 2 – Reference aircraft values [7].

Parameter	Value	Unit
Maximum Take-off Mass	79.0	t
Maximum Landing Mass	67.4	t
Operational Empty Mass	45.0	t
Maximum Fuel Mass	18.7	t
Thrust-to-Weight Ratio	0.31	-

# 2. Conceptual Aircraft Sizing Methodology

This section describes the development of a software package capable of the conceptual sizing of aircraft following the European Aviation Safety Agency's *Certification Specification for Large Aero-* planes (CS-25) [9] and *Easy Access Rules for Air Operations* [10]. The developed package uses a combination of empirical and semi-analytical methods to size "tube-and-wing" style aircraft powered by the combustion of either hydrogen (LH<sub>2</sub>) or kerosene (JA1<sup>2</sup>).

The paper utilises the A320neo as a reference aircraft, with its top-level aircraft requirements (TLARs) and typical masses presented in Tables 1 and 2, respectively. Therefore, the described sizing algorithm is tailored for A320-like aircraft operating on similar missions with a comparable technology level (e.g. the primary structure is made of aluminium alloy), and the algorithm was primarily developed to investigate the effect of fuel type, aspect ratio and the inclusion of a SAH.

# 2.1 Algorithm Overview

The sizing of aircraft is an inherently multi-disciplinary process, and an overview of the algorithm used in this paper is shown in Fig. 2 in the form of an extended design structure matrix (XDSM) [31]. The green blocks on the diagonal represent the analysis of different disciplines, with the numbering of these blocks indicating their execution order. Variables emanating laterally from each discipline represent the outputs other analysis modules depend on, and the orange rounded blocks represent convergence loops. The algorithm presented in Fig. 2 uses two convergence loops, with the inner loop iterating over computationally 'cheap' disciplines, whereas the outer loop iterates over computationally 'expensive' disciplines.

The following subsections outline the methodology and assumptions used in each of the analysis modules, which are based on the content of multiple books [13, 26, 35, 41] and research articles [20, 25, 32–34]. Furthermore, similar - and in many cases more mature - aircraft sizing tools have already been presented in the literature (such as openAD [46], the Aircraft Design Initiator [10], NeoCASS [19], SAUVE [32], and Aviary³). Many of these tools were used as references and inspiration in this work, but the rationale for not starting with these existing tools was driven by the ease of integration

<sup>&</sup>lt;sup>2</sup>JA1 is an abbreviation of Jet A-1 fuel.

<sup>3</sup>https://github.com/OpenMDAO/Aviary [accessed 24/05/2024]

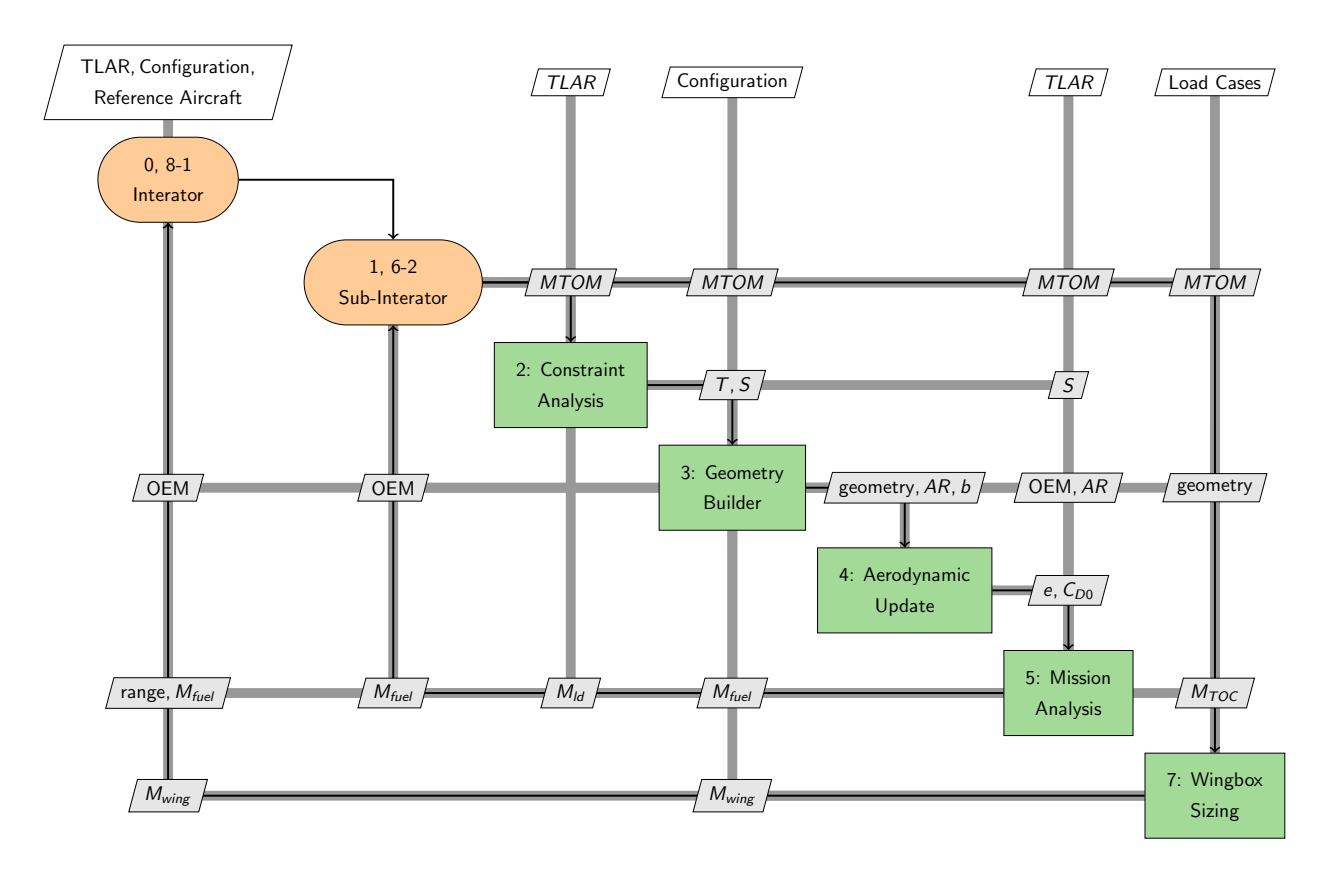


Figure 2 – Extended design structure matrix (XDSM) showing the workflow of the sizing algorithm.

of the wingbox sizing tool described in Section 2.6 which uses MSC Nastran simulations to estimate manoeuvre, gust and turbulence loads.

With all this in mind, the following sub-sections are not intended to provide new insights to the reader. Instead, they aim to offer a transparent understanding of the chosen algorithm, allowing readers to replicate the results and understand the method's strengths and limitations.

# 2.2 Constraint Analysis

A simplified constraint analysis is used in this paper, in which the required wing loading and thrust-to-weight ratio remain constant, with values derived from the reference aircraft (Table 2). Hence, given an assumed maximum landing mass  $(M_{LD})$  and wingspan (b), the required static thrust (T), wing area (S) and aspect ratio (AR) can be calculated.

# 2.3 Geometry and Mass Estimation

Geometry estimation was split into a sequential process, focusing on the fuselage, wing, empennage, propulsion and landing gear. The following subsections outline the method used in each of these processes.

## 2.3.1 Fuselage

The diameter of the aircraft is assumed to be equal to that of the reference aircraft ( $D_{cab} = 2.02 \text{m}$ ), and it is assumed that there are six seats per row, leading to a cabin length of

$$l_{\text{cab}} = 0.7456 \left[ \text{PAX} / 6 \right] \tag{1}$$

where the scaling factor has been approximated from the single class configurations of the A319, A320 and A321 'neo' variants [6–8]. The length of the cockpit,  $l_{cp}$  is assumed to be 4 m and the length of the tail section ( $l_{tail}$ ) is assumed to equal 1.67 times the cabin diameter. It is assumed that the fuel tank is placed in the aft of the fuselage; its outer radius is assumed equal to that of the cabin<sup>4</sup>,

<sup>&</sup>lt;sup>4</sup>an integral tank design [13]

and its length ( $l_{tank}$ ) is calculated according to the required fuel mass ( $M_f$ ) and the process detailed in Section 2.3.2 Therefore, the total length of the fuselage is equal to

$$l_{\text{fus}} = l_{cp} + l_{\text{cab}} + l_{\text{tail}} + l_{\text{tank}} \tag{2}$$

and the mass of the fuselage, furniture, systems and operational items are estimated using equations 8.3, 8.10, 8.9 and 8.1 in [40], respectively, such that

$$m_{fus} = 6.12D_{\text{cab}}^2(l_{\text{fus}} + 1.5) + 31.6D_{\text{cab}}L + 0.14(m_{t,fus} + m_{t,fus})$$
 (3)

$$m_{furn} = 1.22(l_{fus} - l_{tank})D_{cab}(3D_{cab} + 1.5) + 356.8$$
 (4)

$$m_{sys} = (27.5D_{cab} + 15.3)(l_{fus} - l_{tank})$$
 (5)

$$m_{op} = 35.68 \,\text{PAX}$$
 (6)

where all values are in base S.I. units and  $(m_{t,fus} + m_{t,fus})$  is the combined mass of the fuel tank. Note, the characteristic length in Eqs. (4) and (5) has been modified not to include the length of the aft fuel tank, and the final term in Eq. (3) has been added to improve correlations with previous studies, as discussed in section Section 3.

# 2.3.2 Fuel System

As liquid hydrogen must be stored at temperatures below  $20\,\mathrm{K}$ , the fuel tanks require a low surface area to volume ratio and significant thermal insulation to minimise heat transfer rate to the fuel. As liquid hydrogen absorbs energy from the environment, it evaporates, rising into a gaseous upper region of the fuel tank, known as the *ullage*. As more hydrogen evaporates, the pressure of the ullage increases; if this pressure reaches the structural limit of the tank (known as the venting pressure,  $p_{\nu}$ ), the ullage must be vented. Additionally, the minimum pressure of the ullage must also be kept above atmospheric pressure; this prevents air (and moisture) ingress into the fuel tank, which could result in fuel combustion.

Venting pressure and insulation thickness are chosen as trade-offs between tank mass, insulation mass, and hydrogen lost through venting throughout a mission. For this paper, a constant venting pressure of 250 KPa and an insulation thickness of 12 cm will be assumed, which are in line with those estimated in previous studies [33, 38, 43].

The process used to estimate the mass of a hydrogen fuel tank closely follows that of [33]. The shape of  $LH_2$  fuel tanks was assumed to be cylindrical with ellipsoidal end caps with a 2:1 major to minor axis ratio. For a given total length (L), radius (r) and venting pressure, the wall thickness  $(t_s)$  can be estimated as

$$t = SF \frac{(p_v - p_{out})r}{\sigma} \tag{7}$$

where  $p_{out}$  is the external air pressure, SF is the applied safety factor and  $\sigma$  is the wall's allowable stress. For this paper, values obtained by [13] are utilised, in which the maximum allowable stress of an aluminium alloy is assumed to be  $172.4\,\mathrm{MPa}$ . The mass of the tank was then estimated by calculating the volume of the aluminium wall and insulation and multiplying them by their respective densities ( $2840\,\mathrm{kg/m^3}$  and  $32\,\mathrm{kg/m^3}$  [33]).

Given the thickness of the insulation and the tank wall, the total fuel volume can then be calculated, with allowances made for internal equipment (0.6%) and tank contraction (0.9%) [13, 33, 43]. Furthermore, it was assumed the tank was never filled above 97% of capacity, leaving a 3% ullage to allow for controllable increases in ullage pressure due to unforeseen expansion or heating of the fuel [13]. A 4.6 % unusable fuel allowance is also included, which includes a 0.3 % allowance for the volume of fuel in the fuel system and a 4.3% pressurisation fuel allowance, which is an approximation for the amount of gaseous hydrogen required to maintain the minimum pressure in the fuel tank at the end of the longest mission [33].

For a given tank length and diameter, the process outlined in this section fully defines the internal volume and, therefore, the fuel capacity of the tank. However, during aircraft sizing, the problem is inverted, with the required fuel mass being known but not the tank's dimensions; therefore, an iterative process was used to calculate the tank geometry in each instance.

Table 3 – Hinge mass fraction as a function of normalised hinge position. Extracted from [30].

Normalised Spanwise Hinge Position	0.32	0.48	0.64	0.90	1.00
Hinge Mass Fraction $(\tilde{m}_{fold})$	0.116	0.087	0.032	0.010	0.000

Table 4 – CFM-LEAP-1A engine performance characteristics [11].

Parameter	Value	Unit
Thrust (Static)	121	kN
Mass	3008	kg
Length	3.328	m
Diameter	2.4	m
BPR	11	-

# 2.3.3 Wings

The quarter chord sweep angle  $(\Lambda_{qtr})$  is calculated as a function of the cruise mach number  $(M_c)$ , such that [41]

$$\Lambda_{qtr} = \arccos(\frac{3M^*}{4M_c}) \tag{8}$$

where  $M^*$  is the critical Mach number and represents the technology level of the wing design - for this paper, it is set to 0.935. As per the reference aircraft, it is assumed that the trailing edge sweep angle is zero degrees up to a spanwise position of  $3.25 \,\mathrm{m}$  (enabling the integration of landing gear and high lift devices) and the taper ratio outboard of this section is equal to 0.35. The thickness-to-chord ratio at the root ( $t_c$ ) is assumed to be equal to [41]

$$t_c = \cos \Lambda_{atr} (M^* - 0.1(1.1C_{l,TOC}/\cos[2](\Lambda_{atr}))^{1.5} - M_c \cos \Lambda_{atr})$$
(9)

where  $C_{l,TOC}$  is the lift coefficient at the 'top of climb' on the design mission. The tip thickness-to-chord ratio is assumed to be three % lower than that of the root [40].

Overall, Eqs. (8) and (9) and the assumptions mentioned above fully define the planform and general thickness of the wing. The definition of the wing's primary mass and stiffness is detailed in Section 2.6 and the wing's secondary mass is estimated in one of two methods and is assumed to be evenly distributed throughout the wing volume. The first method assumes the secondary mass is 73.7% of the primary mass [20]. The second method uses the component-based approach detailed by Torenbeek [40] and estimates the mass of fixed leading edge, slat, fixed trailing edge, flaps and control surfaces as a function of their planform area (Eqs. (11.63) to (11.67) in [40]). It is assumed that slats occupy 90% of the leading edge, and the flaps and control surfaces occupy 20% and 3% of the total wing area, respectively.

If a GFWT is included, the mass of the hinge mechanism was estimated using the process outlined by Kretov and Tiniakov [30], which captures the increased mass requirements of larger, heavier wingtips. More specifically, Table 3 contains a tabulated version of Fig. 6 in [30]; it describes the variation in the hinge mass fraction (the hinge mass as a percentage of the total wing mass) as a function of its normalised spanwise location, and an Akima spline was used to interpolate between the different values.

# 2.3.4 Propulsion

The CFM-LEAP-1Aturbofann engine was used as the reference engine for this study. Its dimensions, static thrust and mass are shown in Table 4. For a given required thrust, the engine dimensions were scaled according to

$$L = L_{\text{actual}} (T/T_{\text{actual}})^{0.4} \tag{10}$$

$$D = D_{\text{actual}} (T/T_{\text{actual}})^{0.5} \tag{11}$$

$$M = M_{\text{actual}} (T/T_{\text{actual}})^{1.1} \tag{12}$$

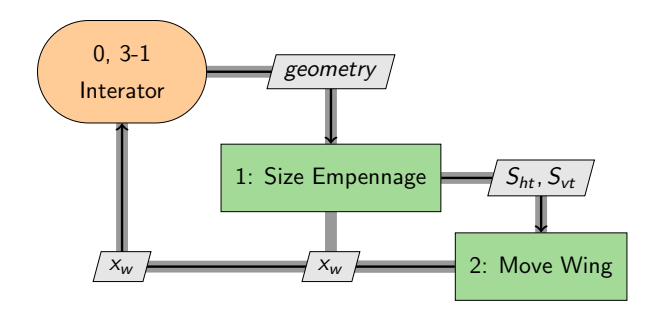


Figure 3 – Empennage sizing XDSM.

Table 5 – Empennage sizing parameters.

Parameter	Value
$ar{V}_{ht}$	0.9936
$ar{V}_{vt}$	0.0706
$x_{ht}$ [m]	$l_{fus} - 0.75c_{ht} - 2$
$x_{vt}$ [m]	$l_{fus} - 0.75c_{vt} - 2$
$AR_{ht}$	4.9
$AR_{vt}$	3.1

which are taken from [35] and where T, L, D and M stand for the thrust, length, diameter and mass, respectively.

Due to a lack of available data, the thrust-specific-fuel-consumption (TSFC) of the reference engine is estimated during max thrust and cruise using

$$TSFC_{T,\text{max}} = 19e^{(-0.12 \text{BPR})}$$
 {mg/Ns} (13)  
 $TSFC_{\text{cruise}} = 25e^{(-0.05 \text{BPR})}$  {mg/Ns} (14)

$$TSFC_{\text{cruise}} = 25e^{(-0.05\,\text{BPR})} \qquad \{mg/Ns\}$$
 (14)

which are taken from [35]. By assuming TSFC<sub>cruise</sub> occurs at the design Mach number and altitude in the TLARs, the scaling approach proposed by Gudmundsson [26] was used to estimate the TSFC at other parts of the flight envelope, such that

$$TSFC(M, alt) = (TSFC_{T,max} + BM)\sqrt{T_{alt}/T_0}$$
(15)

where  $T_0$  is the standard atmospheric temperature at sea-level,  $T_{\rm alt}$  is the atmospheric temperature at the chosen altitude, and B is a constant calculated using Eq. (14). The TSFC is assumed to be independent of the static thrust and does not scale with engine size.

Regarding hydrogen-powered aircraft, in previous research, it has been considered a conservative estimate to assume the energy-specific fuel consumption is constant between kerosene and hydrogen-powered engines [13, 33, 38]. Therefore, the TSFC is scaled by the ratio of specific energies of kerosene and hydrogen (43.2/120 = 0.36). Furthermore, it is assumed that the mass of a hydrogen-powered engine is the same as the equivalent kerosene-powered engine.

# 2.3.5 Landing Gear

The mass of the landing gear was estimated using equations 15.50 and 15.51 in [35], multiplied by a scaling factor  $k_{\text{gear}} = 0.85$ , which was used to improve correlations with previous studies [1, 33].

# 2.3.6 Empennage Planform and Wing Placement

The placement of the main wing and the sizing of the empennage are coupled; hence, their analysis was conducted in an iterative loop, as shown in Fig. 3.

The planform area of the horizontal and vertical tail surfaces ( $S_{ht}$  and  $S_{vt}$ , respectively) was sized using fixed tail volume coefficients ( $\bar{V}_{ht}$  and  $\bar{V}_{vt}$ ) [35], such that

$$S_{ht} = \bar{V}_{ht} \frac{S \cdot \text{MGC}}{x_{ht} - x_{aft}} \tag{16}$$

$$S_{vt} = \bar{V}_{vt} \frac{S \cdot b}{x_{vt} - x_{aft}} \tag{17}$$

where MGC is the mean geometric chord of the main wing<sup>5</sup>,  $x_{aft}$  is the aft-most possible position of the aircraft's centre of mass,  $x_{ht}$  and  $x_{vt}$  represent the longitudinal position of the aerodynamic centres

<sup>&</sup>lt;sup>5</sup>As explained well by [26], the mean geometric chord (MGC) is commonly referred to as the mean aerodynamic chord (MAC). However, the term definition is based solely on geometry and has no direct relation to aerodynamic forces. For example, the spanwise position of the MGC rarely aligns with the spanwise centre of lift. Hence, in this paper, the term MGC is preferred.

Table 6 – Parameters used to estimate the zero-lift drag coefficient for each component. Most values have been estimated using design rules from [35].

Component	p <sub>lam</sub> [%]	FF	Q
Wing	25	Eq. (12.30) [35]	1
Fuselage	$10/37.6 \cdot l_{fus}$	Eq. (12.31) [35]	1
External Store	25	Eq. (12.32) [35]	1.3
Engine	25	Eq. (12.32) [35]	1.3
Empennage	25	Eq. (12.30) [35]	1.04

for the horizontal and vertical tail surfaces, respectively, and .  $\bar{V}_{ht}$ ,  $\bar{V}_{vt}$ ,  $x_{ht}$  and  $x_{vt}$  are approximated from that of the reference aircraft, and the values are shown in Table 5.

The position of the main wing is chosen so that the aft-most achievable position of the aircraft's centre of mass—considering all combinations of fuel and payload—lies at 35% of the MGC (e.g. 10% of the MGC behind the mean aerodynamic centre of the main wing).

# 2.4 Aerodynamic Parameter Estimation

The drag polar of the aircraft is assumed to be of the form

$$C_D = C_{D,0} + \frac{C_L^2}{\pi e_0 \, \text{AR}} \tag{18}$$

where  $C_{D,0}$  is the zero-lift drag coefficient,  $C_L$  is the current lift coefficient, and  $e_0$  is the Oswald efficiency factor.

The Oswald efficiency factor is estimated from a simulation of the aeroelastic model (described in Section 2.6 during steady level flight at the 'top of climb'.

The zero-lift drag coefficient is estimated using the 'component build-up method' and a flat-plate analogy [35], in which  $C_{D,0}$  is calculated as the summation of component level zero-lift drag coefficients, such that

$$C_{D,0} = \sum \left( C_{fe} \cdot \text{FF} \cdot Q \cdot S_{wet} / S_{ref} \right) + C_{D,p}$$
(19)

where  $C_{fe}$  is the skin-friction drag coefficient for each component, FF is the component form factor, Q is an interferance factor and  $S_{wet}$  is the component wetted area.  $C_{D,p}$  is the drag due to protuberances, and it is assumed to be equal to 2% of the total drag [35]. Estimates for the percentage of laminar flow  $(p_{lam})$ , form factor (FF) and the interference factor (Q) for each component are shown in Table 6.

## 2.5 Mission Analysis

The mission analysis module estimates the fuel required to complete a design mission. The chosen design mission is shown in Fig. 4, which adheres to the EASA Rule for Air Operations [10]. The design mission range, cruise altitude, cruise Mach number and alternate range are all specified in the aircraft TLARs. Contingency fuel is calculated as 3% of trip fuel, and the reserve fuel is the fuel required to loiter for 30 minutes above the alternate airport. It should be noted that, unlike other parameters, the alternate range is not specified in the regulations, as the distance to the alternate airport is tailored for each flight plan. This paper used an alternate range of 325 km, which was selected to ensure the reserve fuel of the baseline aircraft (presented in Section 3). matched that of the reference aircraft (which was assumed to be the difference between the maximum landing mass and the zero fuel mass of the aircraft).

The required fuel is estimated using the process outlined by [26], where the aircraft's weight fraction is calculated across each mission segment using the equations outlined in Table 7. The TSFC for each segment was calculated using Eq. (15) at the segment's mean altitude and Mach number. Climb and descent segments were split into smaller segments with a maximum altitude change of  $500 \, \mathrm{ft}$ , and the climb and descent rate was assumed to be  $1500 \, \mathrm{ft/min}$  and  $2000 \, \mathrm{ft/min}$ , respectively.

Once the mission analysis is complete, the weight fraction at critical flight points, such as landing, can be calculated, and the trip fuel,  $M_{f,trip}$ , and the block fuel,  $M_{f,block}$ , can be estimated. The trip fuel is the fuel burned to reach the destination without a diversion, whereas the block fuel is the total fuel required, including reserves.

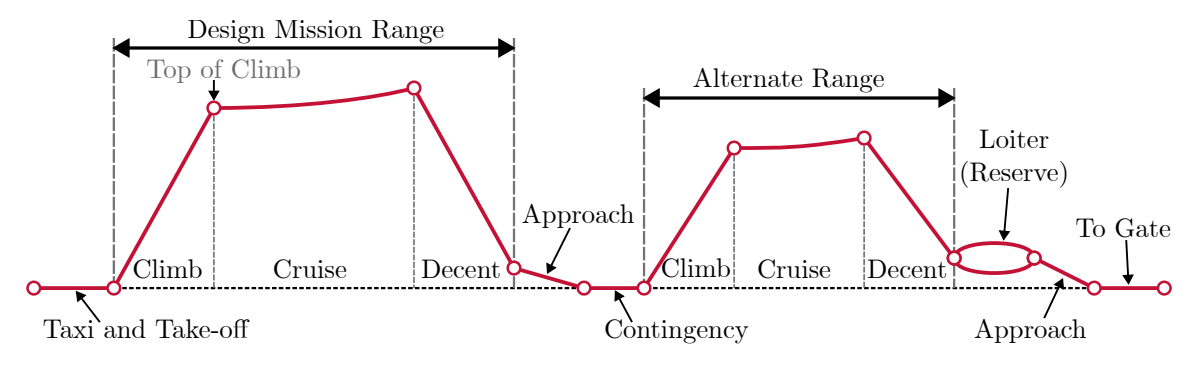


Figure 4 - Design mission segment and fuel breakdown

Table 7 – Mission Segment Equations

Segment	Weight Fraction	Notes
Taxi and Take-off	Equation (6-32) [26]	20 minutes taxi time, 1 minute take off time.
Climb	Equation (6-34) [26]	Split into 500 ft sections
Cruise	Equation (6-35) [26]	Assume constant $C_L$
Decent	Equation (6-34) [26]	Assume idle power (2% thrust-to-weight ratio)
Loiter	Equation (6-36) [26]	-
Contingency	Equation (6-36) [26]	max(3% of trip fuel, 5-minute loiter)

# 2.6 Wingbox Sizing

The wingbox sizing analysis module adapts a procedure previously developed by the authors to size the primary wing structure [25]. An overview of this algorithm is shown in Fig. 5; it uses an aeroelastic model to calculate the forces and moments acting along the wing during manoeuvres, gusts and turbulence encounters. The maximum loads are then used to size the primary elements of the wingbox structure at a discrete number of stations along the wingspan. A condensation process is then used to estimate the bending and torsional rigidity of an equivalent beam model, which is used to update the underlying aeroelastic model. The following subsections detail each stage of the analysis shown in Fig. 5.

## 2.6.1 Aeroelastic Model Generation

The aeroelastic model was generated using MSC Nastran [5]. The structural model is based on a 'stick' and lumped mass representation of an aircraft [45], with the wing discretised into a series of one-dimensional beam elements. As per [16], a hinge was modelled by constraining two coincident nodes - one belonging to the inner wing and one belonging to the wingtip - to have the same translation but free to have different relative rotations with respect to a pre-defined hinge axis.

The aerodynamic forces acting on the reference wing were modelled using an implementation of the doublet lattice method (DLM) [3, 24, 29]. This method is based upon unsteady potential flow theory and reduces to the vortex lattice method (VLM) in the steady case. Although such a method neglects nonlinear aerodynamic effects such as flow separation, shocks and boundary layers, the efficient integration of unsteady aerodynamics terms allows for the efficient evaluation of multiple flight conditions and load cases.

# 2.6.2 Jig Twist Optimisation

The initial aeroelastic model has zero jig-twist, leading to a non-optimal lift distribution during cruise, which increases fuel burn and affects the loads experienced by the wing structure. To remedy this, static aeroelastic analyses are conducted in the steady level flight condition at the top of climb (TOC), with wingtips locked at zero fold angle. After each analysis, the jig-twist required to achieve 1) an elliptical lift distribution and 2) an angle of incidence of 3 degrees is estimated. The process is then repeated until convergence is achieved.

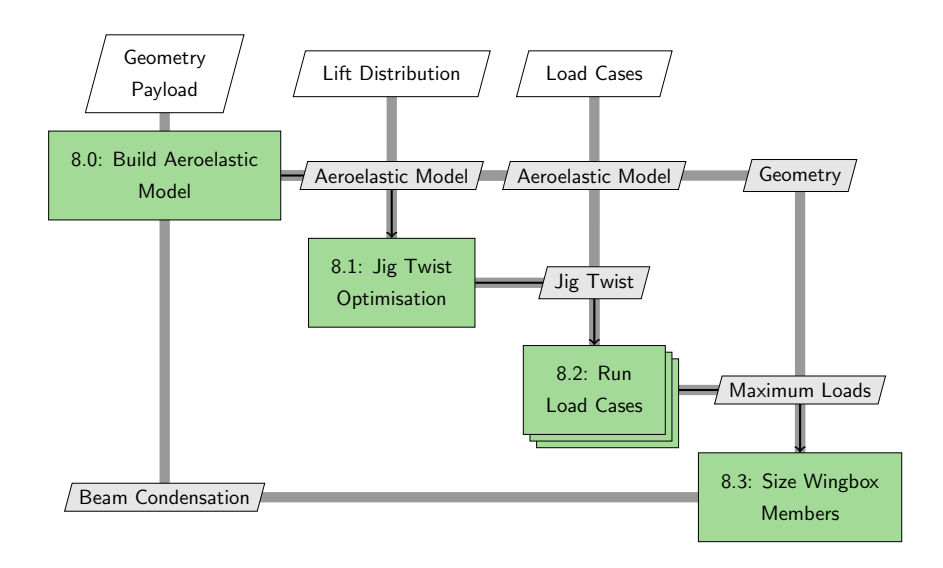


Figure 5 – Extended design structure matrix (XDSM) showing the workflow of the wingbox sizing algorithm.

## 2.6.3 Load Cases

The load cases considered to asses the worst-case loads expected during flight are shown in Table 8. Loads cases 1 to 4 were run for all configurations and included two manoeuvres at the cruise altitude and gust and turbulence encounters at the 'crossover' altitude<sup>6</sup>, at which an aircraft experiences the highest dynamic pressure.

In the case of a configuration including a SAH, load cases 5 to 8 were also simulated. These cases use the same flight conditions as load cases 1 to 4 but represent the failure case in which a SAH remains locked. Typically, a safety factor of 1.5 is applied to the maximum loads experienced by an aircraft [9]. If such a safety factor were applied to the hinge-locked failure case, none of the load alleviation benefits of the SAH would be realised. However, regarding aircraft certification, if less than 1 in every 100,000 flight hours is likely to be spent in a failure condition, a safety factor of 1 can instead be applied to the load case [9](Appendix K). Thus, assuming such reliability levels are attainable with a SAH, a safety factor of 1 is applied to load cases 5 to 8.

Manoeuvre loads were computed by conducting static aeroelastic analysis using the Nastran solution sequence SOL144. Peak gust loads were calculated using the Nastran solution sequence SOL146, where the aircraft was subjected to a family of discrete gusts in the form of a "1-cosine" vertical gust. The selected gust profile was chosen to be the same as that in the EASA regulations regarding civilian aircraft [9], with simulated gust lengths varied between  $18\,\mathrm{m}$  and  $214\,\mathrm{m}$  in 16 linearly spaced increments.

Peak turbulence loads were computed using the Nastran solution sequence SOL146. This analysis is conducted in the frequency domain. It assumes that the power spectral density of the turbulence follows a Von Kármán velocity spectra [9], with a turbulence scale factor of  $2500\,\mathrm{ft}$ . The root-mean-squared (RMS) turbulence intensity is assumed to be  $24.08\,\mathrm{m/s}$  as per [9].

For both gust and turbulence loads, the forces calculated using the SOL146 solution sequence represent incremental loads; therefore, the static aeroelastic loads in steady-level flight must be added to the results.

# 2.6.4 Sizing of Wingbox Members

It is assumed that the front and rear spars are located at 15% and 65% of the chord, respectively. For simplicity, the wingbox is modelled as a rectangle, with a height equal to the mean airfoil thickness between the front and rear spars (assuming the airfoil section is a stretched version of the supercritical aerofoil SC(2)-0614).

<sup>&</sup>lt;sup>6</sup>The crossover altitude is defined as the altitude at which the Mach number and max climb calibrated airspeed, correspond to the same true airspeed

Table 8 – Load cases considered during sizing.

Load Case	Safety Factor	Load Factor	Mode	Mach No.	Altitude	Fuel Level	Hinge
1	1.5	2.5	Manuourve	$M_{c}$	$Alt_c$	$M_{f,TOC}$	Free
2	1.5	2.5	Manuourve	$M_c$	$Alt_c$	0	Free
3	1.5	1	Gusts	$M_c$	Crossover	$M_{f,TOC}$	Free
4	1.5	1	Turbulence	$M_{c}$	Crossover	$M_{f,TOC}$	Free
5	1	2.5	Manuourve	$M_{c}$	$Alt_c$	$M_{f,TOC}$	Locked
6	1	2.5	Manuourve	$M_c$	$Alt_c$	0	Locked
7	1	1	Gusts	$M_c$	Crossover	$M_{f,TOC}$	Locked
8	1	1	Turbulence	$M_c$	Crossover	$M_{f,TOC}$	Locked

Table 9 – Top-level aircraft requirements and selected masses for the A320neo family.

Aircraft		A319 WV055	A320 WV055	A321 WV053
PAX (single class)	[-]	156	180	235
Max. Payload	[t]	17.75	19.3	25
Harmonic Range	[nm]	2720	2450	2500
$(T_W)_{TO}$	[-]	0.32	0.31	0.31
$M_{Lnd}/S$	$[kg/m^2]$	522.1	550.7	631.5
MTOM	[t]	75.5	79	93.5
OEM	[t]	42.6	45.0	50.6
Wing Area	$[m^2]$	122.4	122.4	122.4

Given the maximum bending and shear loads at each beam spanwise station, the wingbox elements (such as spar cap and skin thickness) were sized as detailed in [25]. The process consists of a series of handbook methods which ensure the structure (which is assumed to be constructed of aluminium with a Young's modulus of  $97\,\mathrm{GPa}$ , shear modulus of  $37.3\,\mathrm{GPa}$ , density of  $2710\,\mathrm{kg/m^3}$  and yield stress of  $0.5\,\mathrm{GPa}$ ) can withstand the required loads without buckling. Additionally, a minimum thickness of  $0.5\,\mathrm{mm}$  was set for each element. Following this, the condensation process detailed in Appendix A of [25] was used to estimate the one-dimensional beam properties at each beam station.

# 3. Methdology Validation

To validate the methodology outlined in Section 2, an aircraft was first sized to compare with the reference aircraft, an A320neo. However, even at the conceptual level, sizing an aircraft that matches the reference aircraft's size and performance is a non-trivial process. The A320neo is part of a family of aircraft, including the A319neo and A321neo. Even though the maximum take-off mass varies by up to 18 tonnes between these models, they all share the same wing planform area<sup>7</sup>, empennage and engines<sup>8</sup> [42].

Therefore, the load cases of the A321 must be considered in the sizing of an aircraft equivalent to the A320. To achieve this, an aircraft with the same TLARs as the A321 (Table 9) was first sized, assuming double-slotted Fowler flaps. Then, the properties of the wing, empennage, and engines were held constant, and the sizing algorithm was restarted with the TLARs of the A320 and A319, respectively, now assuming single-slotted Fowler flaps.

A comparison between the A320 family and the conceptual aircraft sized in this manner (the B3xx-JA1, where JA1 stands for Jet A-1 fuel) is shown in Table 10. Note that the wing area was fixed to that of the A321neo, and the fuel capacity of the wings and central fuselage tank was tuned to match the quoted capacities for the A320 (6.5 t in the central tank and 6.1 t in each wing [4]). The accuracy between the reference and sized aircraft (Table 10) is well within those expected at the conceptual design stage.

It is challenging to validate the sizing of liquid-hydrogen-powered aircraft due to the lack of available data. Therefore, the difference between two aircraft sized with the same TLARs but powered with

<sup>&</sup>lt;sup>7</sup>It should be noted that the increased wing loading of the A321 is somewhat compensated by the use of a more complex high-lift system (i.e. a double slotted fowler flap as opposed to a single slotted fowler flap on the A320); additionally some structural strengthening is likely to have been included in key areas.

<sup>&</sup>lt;sup>8</sup>Although the rated static thrust of the A321neo engines is over 20% greater than that used on the A320, the engines are identical. The added thrust reportedly came from a software update [digital link].

Table 10 - Comparison table of the A320neo family and the sized aircraft

Parameter	A321	B321-JA1	$\Delta$ [%]	A320	B320-JA1	Δ[%]	A319	B319-JA1	Δ[%]
$M_{TO}$ [t]	93.5	93.3	0	79.0	78.9	0	75.5	75.6	0
$M_{OEM}$ [t]	50.6	50.8	0	45.0	45.0	0	42.6	42.7	0
$M_{Lnd}$ [t]	77.3	78.3	+1	67.4	66.3	-2	63.9	62.4	-2
$M_{f,cap}$ [t]	18.4	18.7	+2	18.7	18.7	0	18.7	18.7	0
$M_{f,block}$ [t]	17.9	17.4	-3	14.7	14.7	0	15.2	15.1	-1
$M_{f,trip}$ [t]	15.5	15.1	-2	12.7	12.7	0	13.1	13.2	+1
$S[m^2]$	122.4	122.4	0	122.4	122.4	0	122.4	122.4	0
$l_{fus}$ [m]	44.5	44.5	0	37.6	37.1	-1	33.8	34.1	1
$R_{ferry}[km]$	6945	6766	-3	7954	7673	-4	8186	8070	-1

Table 11 – Comparison between the baseline jet fuel and hydrogen-powered aircraft present in [33] and this paper.

Parameter	SMR-JA1-a	SMR-LH2-b	Δ [%]	B320-JA1	B320-LH2-a	Δ [%]
MTOM [t]	79.1	74.8	-5	77.2	73.4	-5
OEM [t]	44.8	49.8	+11	45.0	43.8	-3
$M_{fus}$ [t]	10.6	13.2	+25	10.0	12.4	+24
$M_{wing}$ [t]	10.0	10.0	0	8.1	8.7	+8
$M_{ht} + M_{vt}$ [t]	1.7	2.4	+41	1.5	1.3	-12
$M_{tank,aft}$ [t]	0	1540	-	0.0	1752.0	-
Fuel Sys. Mass [kg]	280	749	+168	344	766	+123
$M_{f,trip}$ [t]	15	5.73	-62	14.3	5.5	-61
$l_{fus}$ [m]	36.1	45.9	+27	36.9	46.7	+26
$S_{wing}$ [m <sup>2</sup> ]	122	127	+4.1%	117.9	124.7	+5.8%
$S_h t$ [m <sup>2</sup> ]	31.7	8.9	+54.2%	28.8	26.4	-8.2%
SEC [kJ/PAX/km]	778	821	+6	653	698	+7

either kerosene or hydrogen will be compared to that from a similar study [33], which also used the A320neo as the reference aircraft.

Firstly, the TLARs of the A320neo (Table 1) were used to size a kerosene-powered aircraft named the B320-JA1-b. A hydrogen-powered aircraft was then sized using the same TLARs and will be referred to as the B320-LH2-a. As the primary aim of this comparison is to validate structural masses, the maximum capacity of the fuel tank is fixed to that of the other study (5.73 tonnes [33]) and the fuel tank has been sized with the same safety factor (1.25), which is lower than the value typically used in this paper (1.5).

Table 11 shows that moving to hydrogen-powered aircraft decreases the MTOM but increases the OEM and specific energy consumption per passenger per km (SEC), with the magnitude of this trend similar in both studies. The mass breakdown in Table 11 shows that this increase in OEM is primarily driven by the fuel tank and fuselage, with the relative increase in all these parameters comparable across the two studies.

### 4. Results

Considering configurations that do not include a hinge mechanism (e.g., a clean wing), increasing the wingspan of the B320-JA1 results in a heavier wing and, therefore, a greater maximum take-off mass (Fig. 6). This increase in mass requires more lift to support in flight and, therefore, generates more drag. The greater lift-to-drag ratio of larger aspect ratios mitigates this increase in drag, and the benefits of an increased lift-to-drag ratio at lower wingspans outweigh the drag penalty due to the increased mass, leading to a reduction in the SEC (Fig. 6).

However, at larger wingspans, the rate of change in the wing mass increases, and the rate of change in the lift-to-drag ratio decreases, meaning an optimal wingspan exists where the increased mass due to an incremental increase in the wingspan cancels out the benefits of an increased lift-to-drag ratio and where, beyond this value, the SEC begins to increase (Fig. 6).

The optimal wingspan is a function of aircraft configuration and sizing methodology. For instance, changes in the mass of a wingbox structure can significantly impact other required aircraft characteristics, such as maximum-take-off thrust and wing area. In literature, these secondary changes

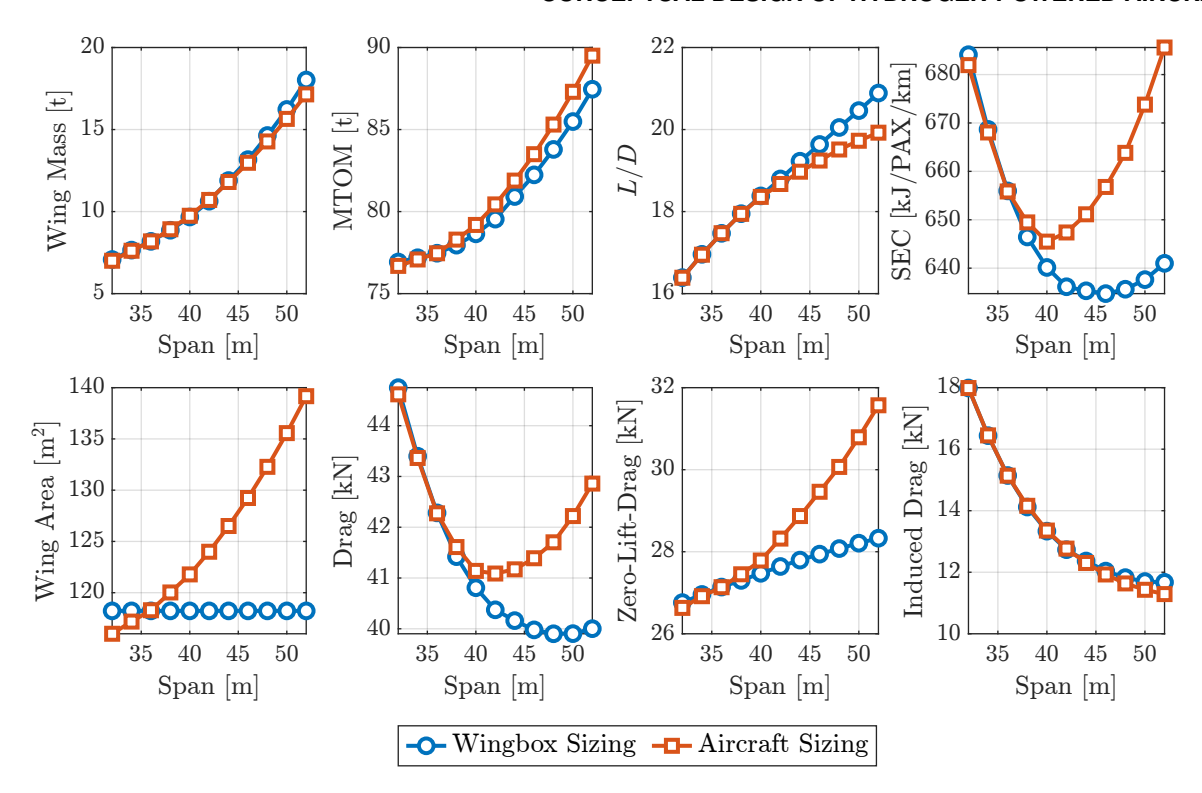


Figure 6 – Variation in selected sized aircraft parameters with wingspan for a kerosene-powered aircraft using either wingbox or aircraft level sizing.

can either be ignored for simplicity (referred to as the wingbox sizing method (WBSM)), such as in previous studies sizing aircraft with a SAH [25] or included in a sizing framework (referred to as an aircraft-level sizing method (ALSM)). The ALSM will result in a heavy aircraft; however, the magnitude of this change and its effect on the aircraft's optimal wingspan and fuel economy is not always apparent.

Fig. 6 shows that both the WBSM and ALSM lead to similar changes in wing mass as the wingspan is increased; however, when using the ALSM, there is an additional increase in the required MTOM (due to, for example, the increased thrust requirements), with approximately an extra  $2.3 \mathrm{m}^2$  of wing area and  $260 \mathrm{\,kg}$  mass required to carry each additional tonne of wing mass. The increased MTOM means the aircraft requires more lift, generating more induced drag, and the increased wing area increases the total skin-friction drag. Overall, when sized with the ALSM, the optimal wingspan is 13% lower than that of an aircraft sized with the WBSM, with a 1.6% greater SEC.

Another important assumption is in the estimation of the wing's secondary mass. The results shown in Fig. 6 use a statistical relationship where the secondary mass is 74% of the primary wing mass. This approach reasonably correlates with previous studies and hand-book equations (Fig. 7). However, these statistical relationships were generated using data from existing aircraft, which typically have an aspect ratio of less than 10. Hence, these methods are likely not well-calibrated to estimate the mass of high aspect ratio wings. For example, consider the WBSM illustrated in Fig. 6. In this model, the secondary mass of the wing increases from 3 tonnes at a wingspan of 32 meters to 7.6 tonnes at a wingspan of 52 meters. Since the wing area remains constant, the average density of the secondary structures more than doubles. Given that these secondary structures are not load-bearing, their specific mass should not change significantly with the size of the aircraft [40]. Therefore, this substantial increase in specific mass appears illogical.

Torenbeek [40] proposes another handbook methodology for estimating the secondary mass, where the fixed and movable leading and trailing edge devices' mass is estimated as a function of their planform area. Fig. 7 shows that both the 'proportional' and 'planform' methods match well at a wingspan of 36m (that of existing similar aircraft), whereas at higher wingspans, the rate of increase in the secondary mass is significantly lower with the planform method, with less than one tonne of additional secondary mass being added between 34 and 52 metres wingspan (compared to 4.7).

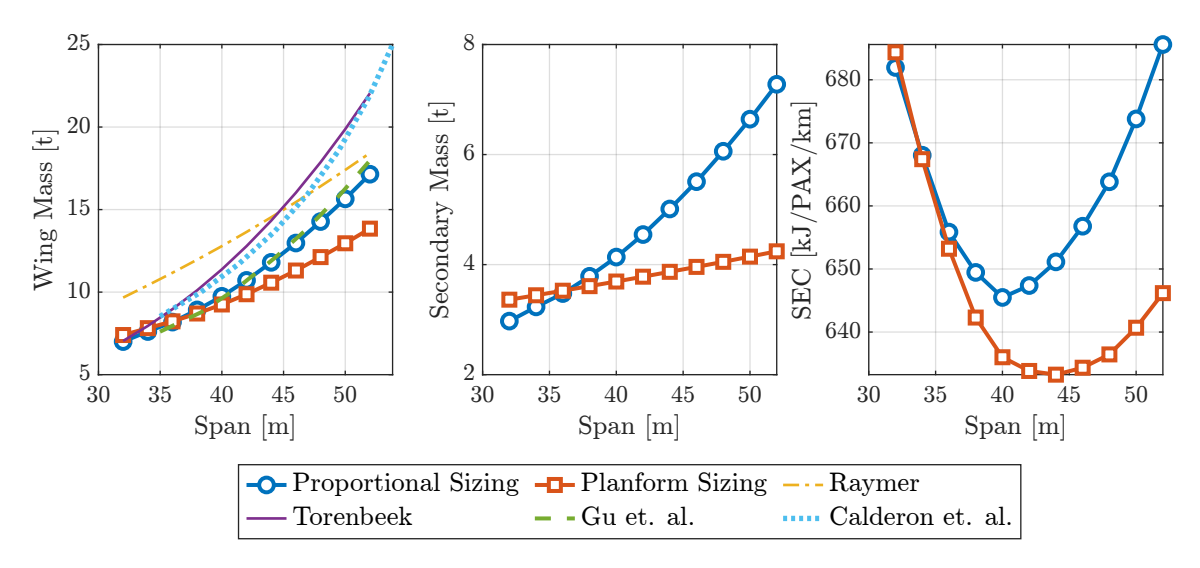


Figure 7 – Variation in selected sized aircraft parameters with wingspan for a kerosene-powered aircraft, using two methods to estimate a wing's secondary mass. The total wing mass is also compared to hand-book equations (Raymer [35] and Torenbeek [40]) and other sizing papers (Gu et al. [25] and Calderon et al. [14]).

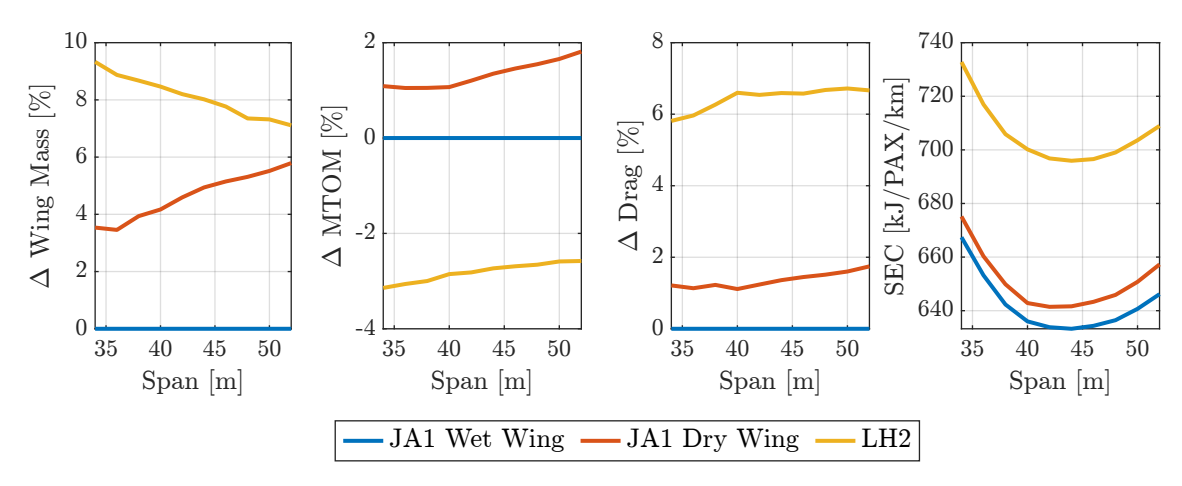


Figure 8 – The delta in selected sized aircraft parameters between a JA1-powered 'wet' wing configuration, and a JA1 'dry' wing and a LH<sub>2</sub> powered dry wing configuration.

tonnes using the proportional method). This reduced growth of the wing mass increases the optimal wingspan from 40 to 44 metres and improves SEC by 2%. Although the authors have little evidence to assess the relative accuracy of both methods to estimate the mass of high aspect ratio wings, it is presumed that the 'planform' method is based upon a more reasonable set of assumptions, hopefully translating to more accurate sensitivities.

These discussions about the level of sizing — whether WBSM or ALSM — or the estimation of secondary mass are not meant to provide definitive solutions. Instead, they are provided to compare the different methodologies commonly used in sizing papers and to begin explaining the wide range of optimal wingspans observed across these studies. However, the aircraft-level sizing method (ALSM) and the 'planform' secondary mass estimation method will be used for the remainder of this paper. Returning to hydrogen-powered aircraft, using LH<sub>2</sub> leads to fuel-free or 'dry' wing configurations. Fig. 8 shows that storing the fuel in the fuselage increases the required wing mass by up to 6% for a kerosene-powered aircraft. This increase in wing mass leads to further increases in the MTOM, generating more drag during cruise and reducing the fuel economy. Furthermore, the rate of growth in wing mass with wingspan is greater in a 'dry' wing configuration, meaning the optimal wingspan, in terms of fuel economy, is reduced from 44 to 42 metres (Fig. 8).

In hydrogen-powered configurations, the issues of 'dry' wings are compounded due to the heavy LH<sub>2</sub> fuel tank, which is assumed to be stored in the fuselage. This fuel tank and the associated increase

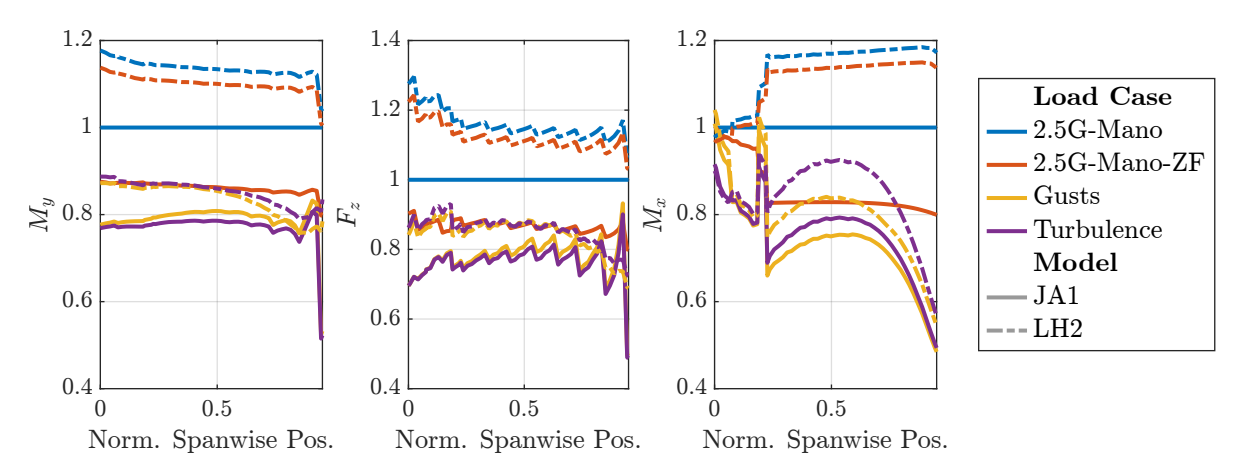


Figure 9 – The spanwise variation in the peak loads during each load case for a JA1 and LH<sub>2</sub> powered aircraft, normalised to the 2.5G manoeuvre loads of the JA1-powered aircraft.

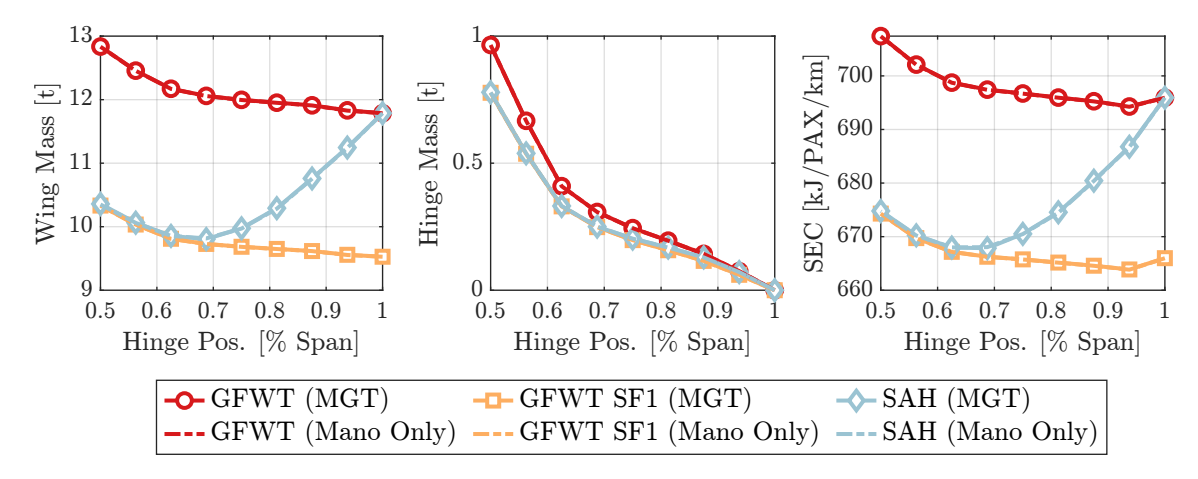


Figure 10 – The variation in selected sized aircraft parameters between three configurations as the spanwise location of the hinge is varied.

in fuselage mass increase the loads experienced by the wings (Fig. 9), raising the required wing mass. Furthermore, the longer fuselage and larger wing area of the LH<sub>2</sub> configuration increase the total drag during cruise, leading to a 10% increase in the SEC when compared to kerosene-powered configurations (Fig. 8).

If it weren't for the current social drive for 'clean' aviation, the increase in SEC for hydrogen-powered aircraft would seem prohibitive, particularly when considering the cost per unit energy of hydrogen is currently higher than that of kerosene and will not be at parity for the foreseeable future [2] (assuming constant taxation policy). However, the uncertain future of fossil fuels, particularly regarding their direct taxation or the taxation of emissions, means that hydrogen-powered aircraft may become a viable alternative, albeit the cost of flying for consumers seems likely to increase.

The aircraft presented so far do not include folding wingtips and, therefore, would not have the same ground wingspan as the current generation of aircraft, limiting their operational flexibility. At a span of 45 metres, Fig. 10 shows the effect of adding a GFWT at different spanwise locations. Starting at the wingtip, as the location of the hinge is moved towards the root, the required hinge mass increases, increasing the total wing mass and reducing the aircraft's fuel economy. For a 45-metre wingspan, a spanwise hinge position of 80% is required to achieve a ground span of 36m, increasing the SEC by 0.3%. It is important to emphasise that an 'ideal' configuration would not use a GFWT; however, if required, the hinge's optimal location is as far outboard as possible.

The required wing mass of an aircraft can be reduced by incorporating load alleviation systems such as the semi-aeroelastic hinge (SAH). When these systems are active, a safety factor of 1.5 must be applied to the measured loads. However, failure cases in which the system is inactive must also be considered. If a failure is likely to occur less than once every 10,000 flight hours, a factor of 1 can

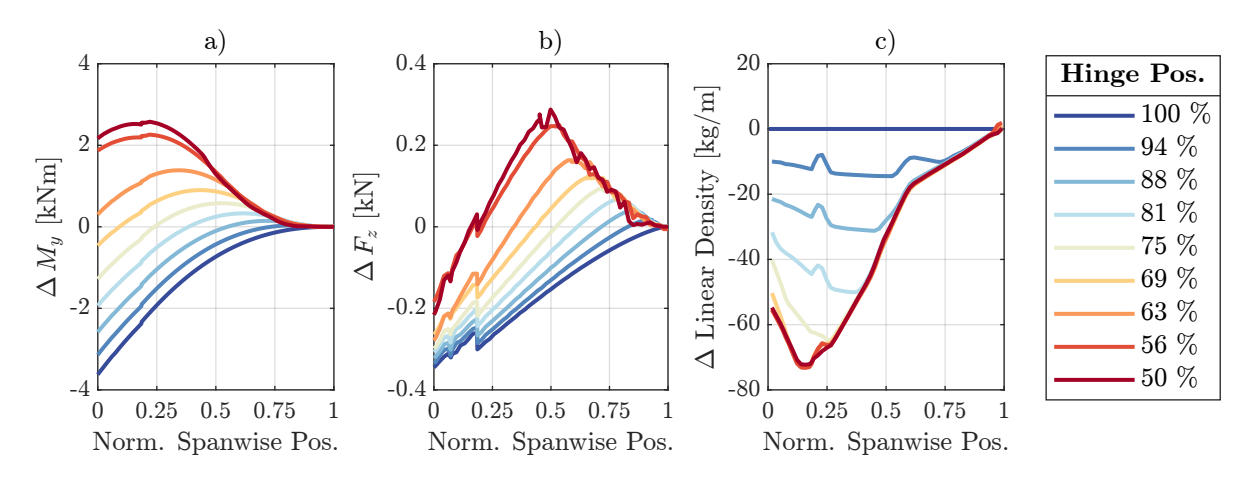


Figure 11 – a) and b), the delta between the spanwise loads during the 'normal' manoeuvre load case and the 'failure' manoeuvre load case. with position values indicating the failure load case is larger. c) the spanwise variation in wingbox linear density.

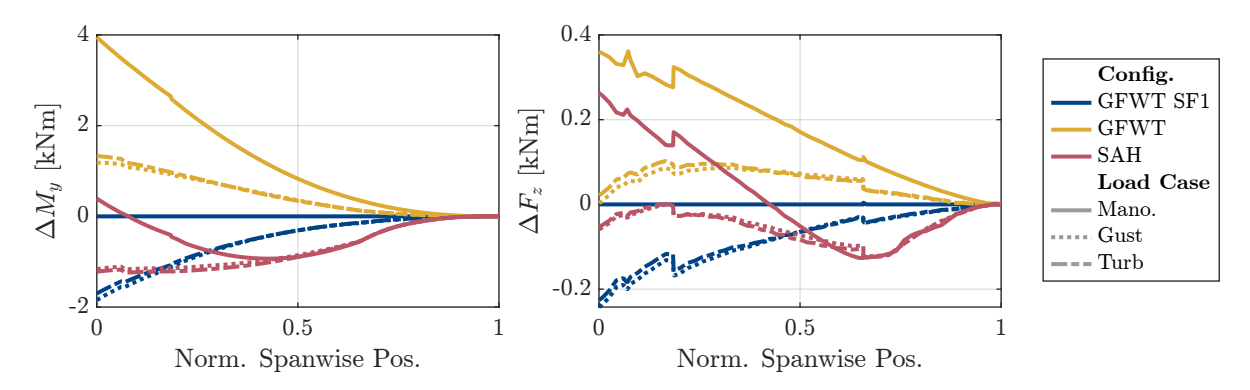


Figure 12 – The spanwise variation in loads between three aircraft configurations with a hinge located at 70% of the span. The loads are normalised to the 'failure' manoeuvre loads.

be applied to these load cases. Therefore, an 'ideal' load alleviation system can reduce the load experienced by an aircraft by 33%. Fig. 10 shows that for a GFWT configuration, an 'ideal' load alleviation system can reduce the wing mass by over two tonnes, leading to a 4.5 % reduction in SEC.

If a GFWT is replaced with a SAH, Fig. 10 shows that reducing the hinge position from 100% to 70% of the span reduces the required wing mass, with the SEC reducing to close to the value of the 'ideal' load alleviation system. As the wingtip size is further increased, the SEC follows the same trend as the 'ideal' system, with an increasing hinge mass increasing the SEC, leading to an optimal wingtip size of approximately 30% of the span.

To explain the occurrence of an 'optimal' hinge position, Fig. 11 a) and b) show the delta between the 'normal' and 'failure' manoeuvre loads (with the safety factors of 1.5 and 1 applied, respectively). In these figures, a negative value means that the largest loads are seen in the 'normal' load case, whereas a positive value means the failure load case is critical. Unsurprisingly, at a hinge position of 100%, the SAH provides zero load alleviation, meaning the 'normal' load case (with a safety factor of 1.5) sizes the entire wing. As the hinge is moved inboard, a greater proportion of the wing is sized by the 'failure' load case; indeed, at a hinge position less than 63% of the span, the 'failure' case determines the critical bending moments across the entire wing. Once the 'failure' case dominates the maximum loads, further reduction in the 'normal' loads by increasing the size of the SAH does not affect the critical loads, meaning there is no reduction in wing mass. Instead, further increases in the size of the SAH increase the hinge mass, increasing the SEC, meaning an 'optimal' spanwise hinge location exists at approximately 70% of the span. Furthermore, Fig. 13 shows that this optimal hinge location remains relatively constant as the total span of the aircraft is varied.

The inclusion of gust and turbulence loads in the sizing process leads to marginal increases in wing

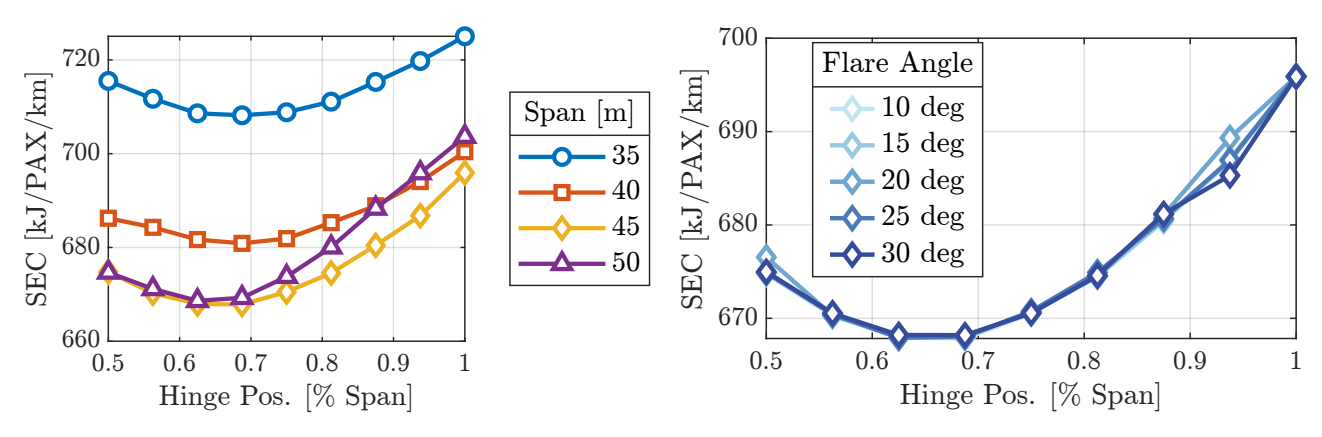


Figure 13 – Variation in the SEC of aircraft using a SAH with different wingspans, as the normalised spanwise hinge position varies.

Figure 14 – Variation in the SEC of aircraft using a SAH with different flare angles, as the normalised spanwise hinge position varies.

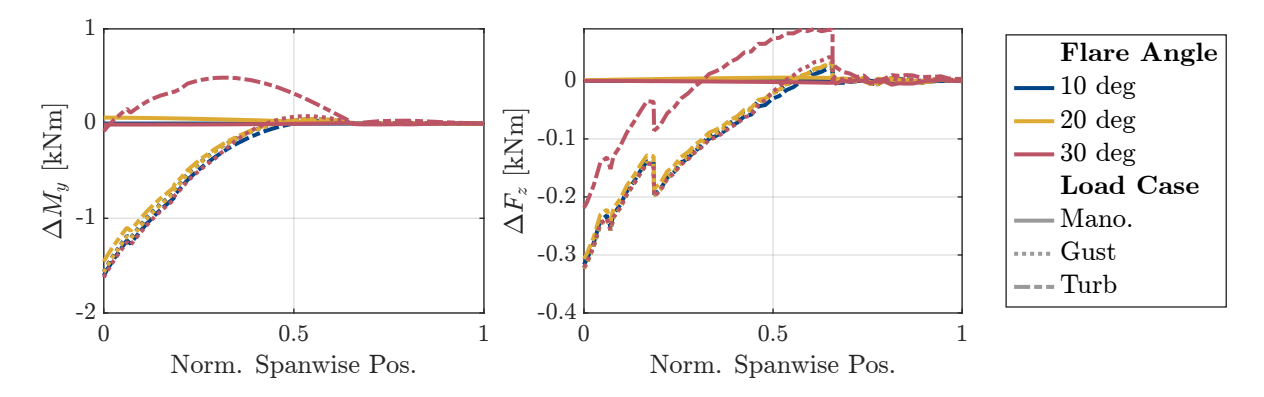


Figure 15 – The spanwise variation in loads between aircraft with different flare angles and a hinge located at 70% of the span. The loads are normalised to the manoeuvre manoeuvre loads of an aircraft with a 10-degree flare angle.

mass and SEC (Fig. 10), which is due to increased loading on outboard sections of the wing (see Fig. 12). However, these increases do not qualitatively change the presented conclusions, with the SAH configuration showing a similar sensitivity to gusts and turbulence as the GFWT configuration. The qualitative insignificance of the dynamics loads suggests that although they are important for the safe design of aircraft, their importance at the conceptual design level may be limited for the configurations considered in this paper.

Another parameter which has previously been identified as important when considering the response of floating wingtips is the flare angle, which, as shown in Fig. 1, describes the angle between the flow direction and the hinge line. Increasing the flare angle increases the aerodynamic stiffness of a floating wingtip [18]; this has been shown to improve their response to gust encounters but can also lead to the early onset of flutter [18]. Fig. 14 shows that the conceptual design methodology used in this paper shows very little sensitivity to flare angle. However, around the 'optimal' wingspan, there is a systematic increase in the wing mass and SEC with flare angle. This increase in mass is primarily due to the rise in peak loads of the turbulence load case (Fig. 15), highlighting that if the sized aircraft was more sensitive to gust and turbulence, the flare angle might have a larger influence on the aircraft total mass.

To summarise the last few paragraphs, the optimal location for a GFWT is as far outboard as possible and for a SAH, it is at around 70% of the wingspan. Fig. 16 shows how these configurations' wing mass and SEC vary with the wingspan. No hinge is present in the 'clean' configuration. In the 'GFWT' and 'SAH' configurations, a hinge is located at a span of 35m (only if the aircraft wingspan is greater than this), and in the 'SAH30' configuration, the hinge is always at 70% of the total span. Fig. 16 shows that using a SAH pushes the optimal wingspan out from 44m to 46m, which corresponds to an aspect ratio of 16.5, and at this optima, the wing mass and SEC are reduced by 20% and 5%,

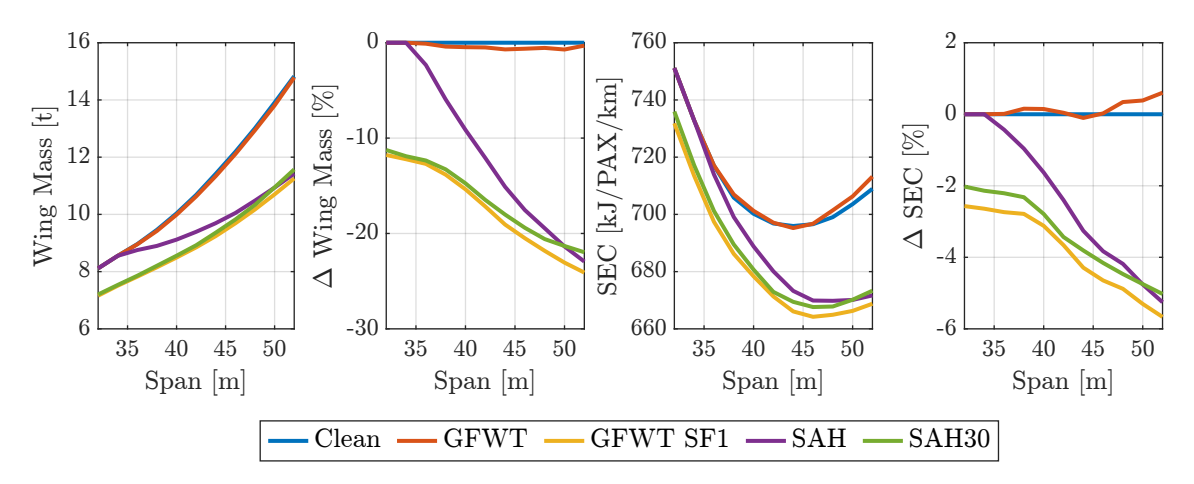


Figure 16 – The variation in the wing mass and SEC of five aircraft configurations, as the wingspan is varied. In the 'clean' configuration, no hinge is present. In the 'GFWT' and 'SAH' configurations, a hinge is located at a span of 35m if the aircraft wingspan is greater than this, and in the 'SAH30' configuration, the hinge is always at 70% of the total span.

respectively, when compared to the GFWT configuration.

However, it should be noted that this analysis holds some large assumptions; for one, it is all linear. Nonlinear deformations reorient the aerodynamic forces, changing the loads applied to the structure. Calderon et al. [14] showed that using linear assumptions on high aspect ratio wings leads to a conservative estimate of the required wing mass, meaning accounting for these effects would likely increase the optimal wingspan and reduce the SEC. Additionally, the analysis in this paper does not consider aeroelastic stability or the flight handling qualities of the aircraft, with future work aiming to include these constraints in the sizing process.

## 5. Conclusions

Hydrogen-powered aircraft present a promising solution to mitigate the aviation industry's environmental impact by eliminating in-flight carbon emissions and significantly reducing the production of nitrogen oxides  $(NO_x)$ . This study develops a conceptual aircraft design methodology to size hydrogen-powered aircraft featuring high aspect ratio wings (HARW) and floating wingtips. Using liquid hydrogen (LH<sub>2</sub>) as a fuel source introduces unique challenges in terms of storage and structural design, as the reduced energy density necessitates larger fuel tanks and results in fuel-free, or 'dry', wings. The developed sizing process uses an aeroelastic model to estimate the loads during manoeuvres, gusts, and turbulence encounters. It shows that moving to dry wings increases the required wing mass by up to 5%, reducing an aircraft's fuel economy. This increase in the wing mass reduces the optimal wingspan of the aircraft, as the required increase in lift-induced drag outweighs the increase in aerodynamic efficiency of larger spans. However, the use of load alleviation devices such as a semi-aeroelastic hinge (SAH) can be used to mitigate the loads seen during manoeuvres, gusts and turbulence encounters and is shown to reduce the wing mass by up to 20% and the fuel economy by 5%. Furthermore, it is shown that the flare angle of the SAH has little effect on the conceptual sizing and using 30% of the wingspan as floating wingtips leads to an optimal configuration, with further increases in wingtip size having no benefit due to the dominance of the 'failure' load cases.

### 6. Contact Author Email Address

j.e.cooper@bristol.ac.uk

# 7. Copyright Statement

The authors confirm that they, and/or their company or organization, hold copyright on all of the original material included in this paper. The authors also confirm that they have obtained permission, from the copyright holder of any third party material included in this paper, to publish it as part of their paper. The authors confirm that

they give permission, or have obtained permission from the copyright holder of this paper, for the publication and distribution of this paper as part of the ICAS proceedings or as individual off-prints from the proceedings.

# Acknowledgements

This work has received financial support from the Innovate UK - Aerospace Technology Institute ONEheart (Out of cycle next-generation highly efficient air transport) project (no 10003388).

#### References

- [1] Abu Salem, K., Palaia, G., Quarta, A. A., and Chiarelli, M. R. (2023). Medium-range aircraft conceptual design from a local air quality and climate change viewpoint. *Energies*, 16(10).
- [2] Adler, E. J. and Martins, J. R. R. A. (2023). Hydrogen-powered aircraft: Fundamental concepts, key technologies, and environmental impacts. *Progress in Aerospace Sciences*, 141:100922.
- [3] Albano, E. and Rodden, W. P. (1969). A doublet-lattice method for calculating lift distributions on oscillating surfaces in subsonic flows. *AIAA Journal*, 7(2):279–285.
- [4] Anon. (2010). A320 flight crew operating manual. Technical report, Airbus S.A.S., Blagnac, France.
- [5] Anon. (2018). Quick Reference Guide. Msc Nastran 2018. MSC Software GmbH.
- [6] Anon. (2020a). A319 aircraft characteristics airport and maintenance planning. Technical report, Airbus S.A.S., Blagnac, France.
- [7] Anon. (2020b). A320 aircraft characteristics airport and maintenance planning. Technical report, Airbus S.A.S., Blagnac, France.
- [8] Anon. (2020c). A321 aircraft characteristics airport and maintenance planning. Technical report, Airbus S.A.S., Blagnac, France.
- [9] Anon. (2020d). Certification specifications and acceptable means of compliance for large aeroplanes cs-25 amendment 26. Technical report, Easa.
- [10] Anon. (2023a). Easy access rules for air operations revision 21. Technical report, Agency, European Union Aviation Safety.
- [11] Anon. (2023b). Type-certification data sheet for engine leap-1a and leap-1c series engines. Technical Report EASA.E.110, European Union Aviation Safety Agency.
- [12] Balatti, D., Haddad Khodaparast, H., Friswell, M. I., Manolesos, M., and Amoozgar, M. (2021). The effect of folding wingtips on the worst-case gust loads of a simplified aircraft model. *Proceedings of the Institution of Mechanical Engineers, Part G: Journal of Aerospace Engineering.*
- [13] Brewer, G. D. (1991). Hydrogen Aircraft Technology. CRC Press, Boca Raton, FL.
- [14] Calderon, D., Cooper, J., Lowenberg, M., Neild, S., and Coetzee, E. (2019). Sizing high-aspect-ratio wings with a geometrically nonlinear beam model. *Journal of Aircraft*, 56(4):1455–1470.
- [15] Carrillo, X., Mertens, C., Sciacchitano, A., Van Oudheusden, B., De Breuker, R., and Sodja, J. (2022). Wing stiffness and hinge release threshold effects on folding wingtip gust load alleviation. AIAA SciTech 2022 Forum.
- [16] Castrichini, A. (2017). *Parametric Assessment of a Folding Wing-Tip Device for Aircraft Loads Alleviation*. PhD thesis, University of Bristol.
- [17] Castrichini, A., Hodigere Siddaramaiah, V., Calderon, D. E., Cooper, J. E., Wilson, T., and Lemmens, Y. (2016). Nonlinear folding wing tips for gust loads alleviation. *Journal of Aircraft*, 53(5):1391–1399.

- [18] Castrichini, A., Siddaramaiah, V. H., Calderon, D. E., Cooper, J. E., Wilson, T., and Lemmens, Y. (2017). Preliminary investigation of use of flexible folding wing tips for static and dynamic load alleviation. *The Aeronautical Journal*, 121(1235):73–94.
- [19] Cavagna, L., Ricci, S., and Travaglini, L. (2011). Neocass: An integrated tool for structural sizing, aeroelastic analysis and mdo at conceptual design level. *Progress in Aerospace Sciences*, 47(8):621–635.
- [20] Chambers, M. C., Ardema, M. D., Patron, A. P., Hahn, A. S., Miura, H., and Moore, M. D. (1996). Analytical fuselage and wing weight estimation of transport aircraft. Technical Report NASA-TM-110392, NASA.
- [21] Cheung, R. C. M., Rezgui, D., Cooper, J. E., and Wilson, T. (2018). Testing of a hinged wingtip device for gust loads alleviation. *Journal of Aircraft*, 55(5):2050–2067.
- [22] Cheung, R. C. M., Rezgui, D., Cooper, J. E., and Wilson, T. (2020). Testing of folding wingtip for gust load alleviation of flexible high-aspect-ratio wing. *Journal of Aircraft*, pages 1–13.
- [23] Fezans, N., Joos, H.-D., and Deiler, C. (2019). Gust load alleviation for a long-range aircraft with and without anticipation. *CEAS Aeronautical Journal*, 10(4):1033–1057.
- [24] Giesing, J. P., Kalman, T. P., and Rodden, W. P. (1972). Subsonic steady and oscillatory aero-dynamics for multiple interfering wings and bodies. *Journal of Aircraft*, 9(10):693–702.
- [25] Gu, H., Healy, F., Rezgui, D., and Cooper, J. (2022). Sizing of high-aspect-ratio wings with folding wingtips. *Journal of Aircraft*, pages 1–15.
- [26] Gudmundsson, S. (2021). *General Aviation Aircraft Design: Applied Methods and Procedures*. Butterworth-Heinemann, Oxford, England.
- [27] Healy, F. (2024). The Impact of Geometric Nonlinearities on the Behaviour of Floating Wingtips. PhD thesis, University of Bristol.
- [28] Healy, F., Pontillo, A., Rezgui, D., Cooper, J. E., Kirk, J., Wilson, T., and Castrichini, A. (2021). Experimental analysis of the dynamics of flared folding wingtips via a novel tethered flight test. San Diego, California, USA. AIAA SCITECH 2022 Forum.
- [29] Kalman, T. P., Rodden, W. P., and Giesing, J. P. (1971). Application of the doublet-lattice method to nonplanar configurations in subsonic flow. *Journal of Aircraft*, 8(6):406–413.
- [30] Kretov, A. and Tiniakov, D. (2022). Evaluation of the mass and aerodynamic efficiency of a high aspect ratio wing for prospective passenger aircraft. Aerospace, 9(9):497.
- [31] Lambe, A. B. and Martins, J. R. A. (2012). Extensions to the design structure matrix for the description of multidisciplinary design, analysis, and optimization processes. *Structural and Multidisciplinary Optimization*, 46(2):273–284.
- [32] Lukaczyk, T. W., Wendorff, A. D., Colonno, M., Economon, T. D., Alonso, J. J., Orra, T. H., and Ilario, C. (2015). *Suave: An Open-Source Environment for Multi-Fidelity Conceptual Vehicle Design*. Aiaa Aviation Forum. American Institute of Aeronautics and Astronautics.
- [33] Onorato, G., Proesmans, P., and Hoogreef, M. F. M. (2022). Assessment of hydrogen transport aircraft. *CEAS Aeronautical Journal*, 13(4):813–845.
- [34] Proesmans, P.-J. and Vos, R. (2022). Airplane design optimization for minimal global warming impact. *Journal of Aircraft*, 59(5):1363–1381.
- [35] Raymer, D. P. (2018). *Aircraft Design: A Conceptual Approach*. Aiaa Education Series. American Institute of Aeronautics and Astronautics, Reston, VA, 6 edition.

### CONCEPTUAL DESIGN OF HYDROGEN-POWERED AIRCRAFT

- [36] Regan, C. and Jutte, C. (2012). Survey of applications of active control technology for gust alleviation and new challenges for lighter-weight aircraft. Technical report, NASA.
- [37] Shirk, M. H., Hertz, T. J., and Weisshaar, T. A. (1986). Aeroelastic tailoring theory, practice, and promise. *Journal of Aircraft*, 23(1):6–18.
- [38] Silberhorn, D., Atanasov, G., Walther, J.-N., and Zill, T. (2019). Assessment of hydrogen fuel tank integration at aircraft level.
- [39] Soreide, D., Bogue, R. K., Ehernberger, L., and Bagley, H. (1996). Coherent lidar turbulence measurement for gust load alleviation. Technical report, NASA.
- [40] Torenbeek, E. (1982). *Synthesis of Subsonic Airplane Design*. Kluwer Academic, Dordrecht, Netherlands, 1982 edition.
- [41] Torenbeek, E. (2013). *Advanced Aircraft Design*. Aerospace Series. John Wiley and Sons, Nashville, TN.
- [42] Van Heerden, A. S. J., Guenov, M. D., and Molina-Cristóbal, A. (2019). Evolvability and design reuse in civil jet transport aircraft. *Progress in Aerospace Sciences*, 108:121–155.
- [43] Verstraete, D., Hendrick, P., Pilidis, P., and Ramsden, K. (2010). Hydrogen fuel tanks for subsonic transport aircraft. *International Journal of Hydrogen Energy*, 35(20):11085–11098.
- [44] Weisshaar, T. A. (1981). Aeroelastic tailoring of forward swept composite wings. *Journal of Aircraft*, 18(8):669–676.
- [45] Wright, J. and Cooper, J. E. (2015). *Introduction to Aircraft Aeroelasticity and Loads*. Aerospace Series. Wiley, Chichester UK.
- [46] Wöhler, S., Atanasov, G., Silberhorn, D., Fröhler, B. M. H. J., and Zill, T. (2020). Preliminary aircaft design within a multidisciplinary and multifidelity design environment.